Journal of Structural Dynamics, 2, (pp. 82-104) 2023
Masing Manifolds: Reconciling the Masing Conditions with Real Hysteresis in Jointed Structures

Journal of
Structural
Dynamics

Masing Manifolds: Reconciling the Masing Conditions with Real Hysteresis in Jointed Structures

M. R. W. Brake*[1], J. H. Porter[1], and M. M. Karpov[1]

[1] *William Marsh Rice University, 6100 Main St., Houston, TX 77005, USA*

Abstract

The Masing conditions establish a criterion to relate the loading curve of a hysteretic system (e.g., systems with friction or plasticity) to its complete hysteresis loop. For the field of joint mechanics, where hysteretic models are often used to describe the dissipative, tangential behavior within an interface, the Masing conditions allow for significant computational savings when the normal load is constant. In practice, though, jointed systems experience time varying normal forces that modify the tangential behavior of the system. Consequently, the hysteretic behavior of jointed structures do not adhere to the Masing conditions. In this work, this discrepancy between the Masing conditions and behavior exhibited by jointed structures is explored, and it is hypothesized that if the Masing conditions accounted for variations in normal force, then they would more accurately represent jointed structures. A new set of conditions is introduced to the original set of Masing conditions, yielding a "Masing manifold" that spans the tangential displacement-tangential force-normal force space. Both a simple harmonic oscillator and a built-up structure are investigated for the case of elastic dry friction, and the results show that the hysteresis of both of these systems conforms to the three dimensional Masing manifold exactly, provided that a set of constraints are satisfied, even though the hysteresis does not conform with the original Masing conditions.

Keywords: Jointed Structures; Tribomechadynamics; Structural Dynamics; Masing Conditions; Hysteresis

---

Received on November 10, 2022, Accepted on October 10, 2023, Published on November 7, 2023

1 Introduction and Context

Jointed structures are ubiquitous in modern engineering. As two components are joined together, the resulting interface exhibits nonlinear, hysteretic behavior. This behavior can change the stiffness and significantly change the damping characteristics of a system as the excitation of the joint is increased [1, 2, 3]. The added damping of jointed interfaces can have significant ramifications depending on the application area. For engines and aeroturbines in particular, damping due to joints can lead to parasitic energy losses that decrease the efficiency of the engine, increase fuel consumption, and ultimately generate more greenhouse gasses that contribute to climate change [4, 5, 2]. In this and other contexts, the dissipation at an interface can significantly increase the likelihood of a part failing due to fretting fatigue [6, 7, 8, 9].

Understanding the exact physics of the frictional interactions within the interface is an open challenge [10, 9]. Recent experiments have shed new light on the physics of the interface that challenge many of the commonly held assumptions for modeling jointed structures. In particular, high speed digital image correlation experiments [11, 12, 13, 14] have demonstrated that the interface itself is dynamically active during excitation, exhibiting opening and closing behavior that invalidates the previous modeling assumption that the interface kinematics can be regularized

---

*brake@rice.edu

[15]. These observations were followed by direct measurements of the contact pressure within the interface [16], which showed that areas within the interface that had previously been assumed to be stuck exhibited significant pressure fluctuations during dynamic excitation (e.g., see the assumptions behind the modeling approaches evaluated in [17]). The bolts are a dynamic component of the system that fluctuate in the load that they carry during dynamic excitation [18, 19], leading to the interface exhibiting significant time and position dependent fluctuations in normal contact pressure, as verified by high fidelity computational models [20, 21, 22].

The fidelity of modeling approaches representing these experimental observations has been mixed. The modeling of jointed interfaces can be conceptually divided into time domain (e.g., transient) and frequency domain (including quasi-static) applications. While there are many similarities between the two domains, the modeling of jointed interfaces in both the frequency domain (e.g., such as by the use of the Harmonic Balance method [23, 24, 25, 26, 27, 17] or the Extended Periodic Motion Concept [28] to study systems with frictional interfaces) and the quasi-static domain [29, 30, 31, 32] has mostly exploited the Masing conditions in order to make computations more tractable and efficient. These simulation methods assume that the system is being driven at a single frequency (usually, excluding multi-harmonic balance methods [23, 33, 26]), that it is oscillating between two extrema, and that the hysteretic behavior is symmetric for the forward and backward loading conditions. Higher harmonics and transient effects are thus neglected. For the most part, these models assume a constant normal force across the interface; however, this over-simplifies the interfacial physics and leads to erroneous predictions of a system's response [19, 21]. While more realistic modeling approaches do exist [34, 35, 36, 21, 37, 22], they tend to be less computationally efficient as they are incompatible with the assumptions of the Masing conditions.

1.1 The Masing Conditions

The Masing conditions [38, 39, 2, 40] stipulate that, for steady state responses, the hysteretic behavior of a system can be uniquely determined from the loading curve formed by taking a system at rest and loading it to its maximum steady state displacement. This loading curve is related to the steady state hysteresis loop via:

1. The forward portion of the hysteresis loop is identical to the initial loading curve except that it is scaled by a factor of two in both displacement and force such that it begins at the smallest displacement and extends to the largest displacement (which is typically from $-u_{max}$ to $+u_{max}$).
2. The reverse portion of the hysteresis loop is identical to the forward portion, only rotated 180° with respect to the center of the hysteresis loop.
3. The hysteretic response is determined from the last point of the loading cycle before a reversal; if the loading curve crosses a previous loading curve, then it must conform to the previous loading curve.

These conditions are illustrated in Fig. 1.

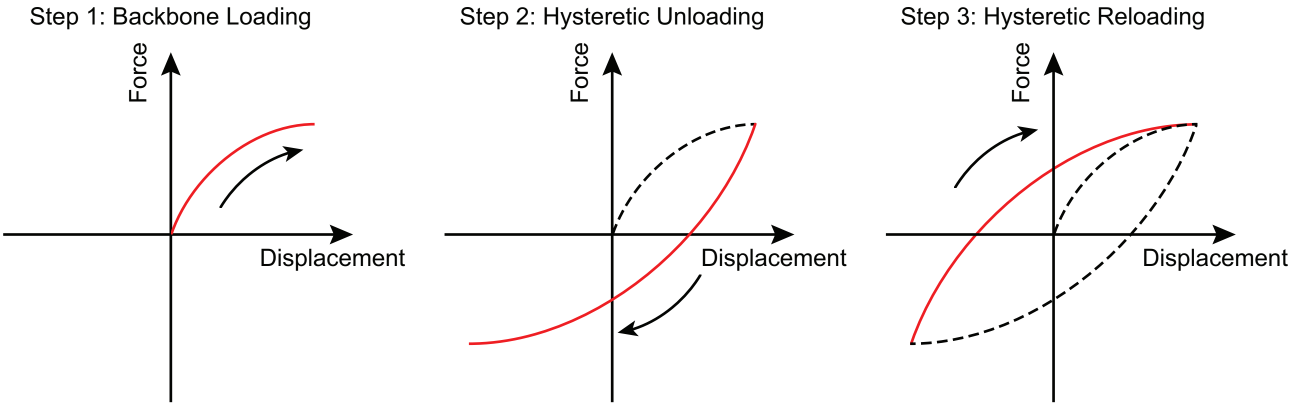

Fig. 1: Illustration of the Masing conditions. The curves in steps two and three are scaled (and rotated) versions of the curve in step one.

The use of the Masing conditions greatly simplifies the calculation of hysteretic behavior as only the initial loading curve needs to be calculated in order to deduce the entire hysteresis loop. In particular, this is the fundamental concept behind the use of quasi-static modal analysis [41, 31] for calculating the hysterestic behavior of a jointed system. If the Masing conditions cannot be used, then it can be at least five times more expensive to calculate the hysteretic behavior of a system using a quasi-static solver [32, 37] as the initial loading curve, first unloading curve, and first reloading curve all need to be calculated. This is the difference between only calculating the curve shown in step one of Fig. 1 and calculating all of the curves shown in steps one, two, and three of Fig. 1.

1.2 Breakdown of the Masing Conditions

In real jointed structures, the normal force across an interface is known to vary during excitation [16, 20]. Further, depending on the microscale topology, the interface can even lose contact at its edges [11] (in which case the normal force goes to zero). As a result, the tangential friction force, which is often conceptualized as being related to the normal force by a scalar (i.e., Coulomb's friction coefficient, μ), is modulated during excitation. This can result in non-symmetric hysteresis loops that violate Masing's conditions, such as shown in Fig. 2. The hysteresis loops in Fig. 2 are calculated using a tribomechadynamics model of the interface [19, 37, 42], and further details of how the system is modeled are found in §4.

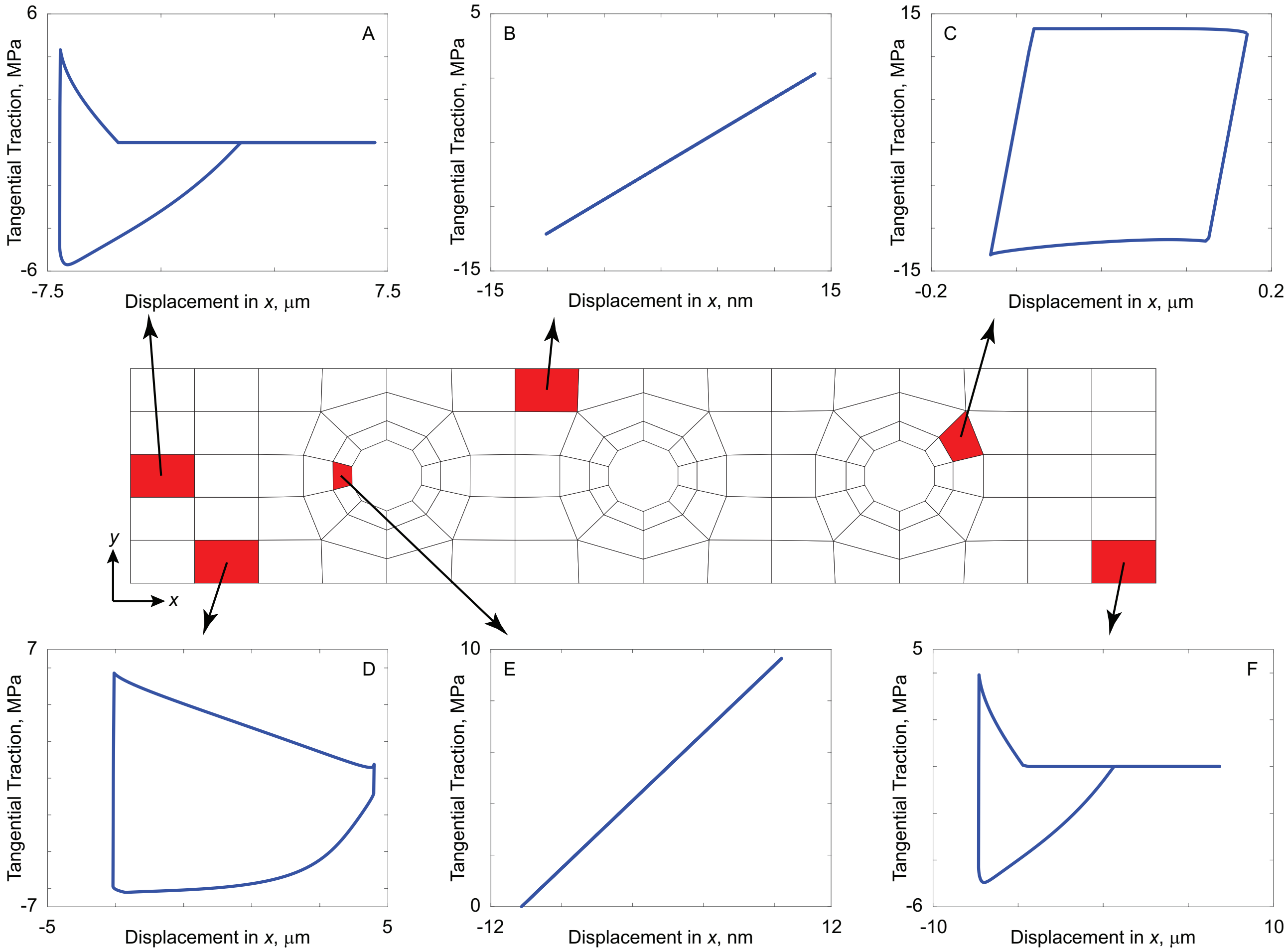

Fig. 2: Hysteresis loops from a tribomechadynamics model of a jointed interface in which the normal load is allowed to vary throughout the simulation due to the external excitation. The reduced order mesh of the interface is shown in the center, and the hysteresis loops for six highlighted elements are shown on the periphery. Note that the displacement is relative, and the scales for each hysteresis loop are different. Labels for each hysteresis loop are provided for reference in §4.

Of the six hysteresis loops shown in Fig. 2, all of the hysteresis loops except B and E clearly violate the Masing conditions (which give rise to symmetric hysteresis loops, an example of which is shown in Fig. 1). To detail some of the break-downs in Masing conditions, if any of these curves were to be in compliance with the Masing conditions, they would need to be parallelograms given the nearly linear loading curves that each exhibits. Likewise, the slip force for a Masing condition-congruent elastic dry friction model must be constant, not decreasing as clearly observed for curves A, D, and F. These discrepancies are further highlighted in Fig. 3.

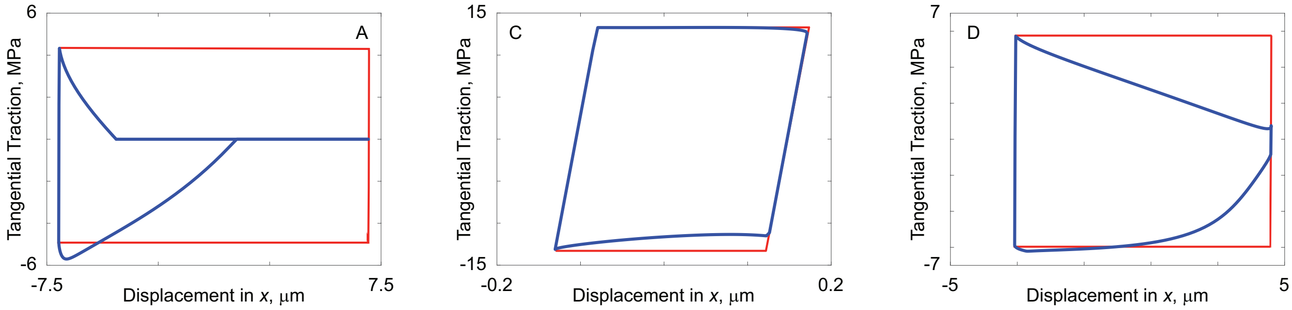

Fig. 3: Details of how two of the hysteresis loops from Fig. 2 violate the Masing conditions; the Masing condition-derived hysteresis loops are shown in red, whereas the true hysteresis loops are shown in blue.

At the elemental level, the hysteretic model for the loops shown in Fig. 2 are described by elastic dry friction (schematically shown in Fig. 4). Similar to a Jenkins element, elastic dry friction is defined as

$$f = \begin{cases} \underbrace{k_T\left(u(t) - u_0\right) + f_0}_{f_{stuck}} & |f_{stuck}| < \mu N(t) \\ \mu N(t)\, \text{sign}\left(f_{stuck}\right) & \text{Otherwise} \end{cases}, \tag{1}$$

in terms of the tangential stiffness k_T, displacement u, time t, normal force N, and having conditions at the previous time instant indicated by subscript $_0$. As $\mu N(t)$ is non-constant, this results in a hysteresis loop that can collapse (i.e., go to zero as the interface separates), have sudden spikes (e.g., when a pressure wave propagates across the interface), or even exhibit a slip force that decreases with time for one portion of the loading curve but not the other (e.g., the bottom left hysteresis loop in Fig. 2). These observations lead to the hypothesis:

> **Hypothesis:** Hysteretic models that satisfy the Masing conditions for constant N will conform to a three-dimensional manifold in u-f-N space when N is varied.

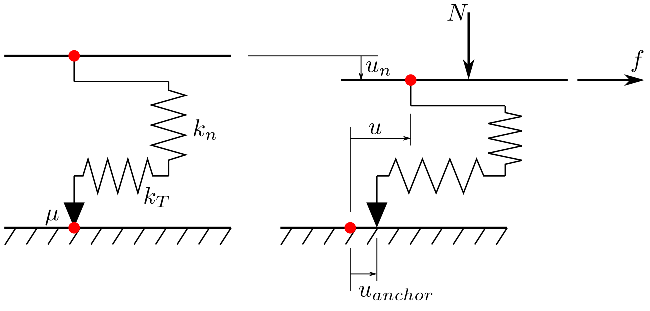

(a) (b)

Fig. 4: Schematic of elastic dry friction model for (a) initial undeformed state of barely in contact and (b) loaded state. In (a) μ, k_T, and k_n are the friction coefficient, tangential stiffness, and normal stiffness respectively. In (b), u_n, u, and u_{anchor} are the displacements in the normal direction, tangential direction, and for the slider in the tangential direction respectively. The applied normal force is N and the frictional tangential force is f. The circles denote references points fixed to each surface.

If this hypothesis is supported, then the modified Masing conditions would result in a response manifold that governed the hysteretic, steady-state behavior of a system. A two-dimensional section of this manifold for a constant normal force would result in the original Masing conditions. However, once the normal force begins to vary, the tangential force-displacement response must be extended into the third dimension, normal force. A ramification of this hypothesis would be a more efficient and accurate method to represent hysteretic behavior in real, jointed structures.

In what follows, the theoretical criteria to construct a Masing manifold are presented in §2. The efficacy of the Masing manifold is then tested in §3 on a simple one degree of freedom oscillator and then in §4 on the model of a built-up structure. Here, the Masing manifold is only considered for elastic dry friction as this research is focused on defining and demonstrating the concept. Finally, conclusions are presented in §5.

2 Construction of the Masing Manifold

A Masing manifold is defined as the three dimensional surface constructed by calculating the hysteresis observed for steady state, single harmonic oscillation between two extrema as a function of N, such as shown in Fig. 5. The specific shape of the Masing manifold is dependent upon the friction model employed. Here, for simplicity, only the elastic dry friction model is considered. The Masing manifold for the elastic dry friction model is constructed from hysteresis loops corresponding to fixing every possible value of N as a constant and applying the Masing conditions independently for each value of N[1]. After reversal the system is stuck, and thus a portion of the manifold consists of a plane that projects down to a single line in the u-f plane with slope k_T. This plane results from the history variables for displacement and force (u_0 and f_0 respectively) in Eq. 1 being able to be rewritten as a single history variable for any given time instant. Specifically, an anchor position is defined to be the history variable displacement that would correspond to the same frictional evaluation if the history force was zero. By rearranging Eq. 1, the anchor position for a given set of history variables is calculated as

$$u_{anchor} = u_0 - f_0/k_T. \tag{2}$$

This quantity is visually represented in Fig. 4. The plane intersects zero tangential force at displacement

$$u_{max,anchor} = u(t_{max}) - \mu N(t_{max})/k_T \tag{3}$$

or

$$u_{min,anchor} = u(t_{min}) + \mu N(t_{min})/k_T \tag{4}$$

for times t_{min} and t_{max} corresponding to the time of minimum and maximum displacement[2], respectively. Here, different signs must be introduced for the maximum and minimum cases since the sign of f_0 is positive or negative respectively. Without a loss of generality, the displacements can be offset such that the anchor displacements $u_{anchor,amp}$ are equal magnitude as defined via

$$u_{anchor,amp} = \begin{cases} (u_{max,anchor} + u_{min,anchor})/2 & u_{max,anchor} + u_{min,anchor} > 0 \\ 0 & Otherwise. \end{cases} \tag{5}$$

In Fig. 5, $\pm u_{anchor,amp}$ are points A and B. The stuck planes (ACE and BDF) are defined by

$$f = k_T(u \pm u_{anchor,amp}). \tag{6}$$

The rest of the manifold then connects the two stuck planes with two planes defined by the slip limits in the positive and negative directions. Six points connected by planes define the manifold:

- The first two points (A and B) are located in the $N = 0$ plane along the line for $f = 0$ at displacements $\pm u_{anchor,amp}$;
- The second two points (C and D) are the limits of macroslip, located at the extremes of displacement $(\pm(u_{anchor,amp} + \mu N_{\max}/k_T))$, the maximum normal force $(N_{\max})$, and the slip force $(\pm\mu N_{\max})$;
- The last two points (E and F) are defined by the onset of macroslip, located at a displacements $\pm(u_{anchor,amp} - \mu N_{\max}/k_T)$, maximum normal force $(N_{\max})$, and slip force $(\mp\mu N_{\max})$.

For the elastic case, $u_{anchor} = 0$ and the last two sets of points become identical resulting in a triangle on a plane for the manifold. The surface defined here describes possible relationships between the displacement, u, tangential force f, and normal force N. The tangential force is constrained to lie on this surface when the Masing manifold is valid. The surface is defined for a specific periodic history of the displacement u and implicitly incorporates the history variables without needing to explicitly include them in calculations. This is one of the key contributions of the Masing manifold for calculating the hysteretic response of a friction element. Because the manifold establishes a set of constraints for how f can change with u and N, it removes the need for a state variable that records the history of

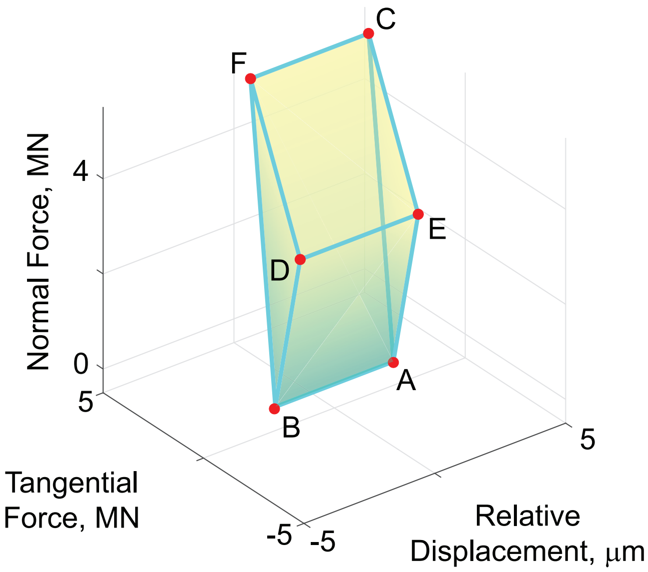

Fig. 5: Example of the construction of a Masing manifold for elastic dry friction with the six points labeled as A through F. Note that the top surface of the manifold, the quadrilateral DECF, is not part of the manifold itself, but rather a surface made by cutting the manifold at some maximum N for visualization purposes.

the system. Consequently, this opens several new opportunities for how frictional responses can be calculated more efficiently, as discussed in subsequent sections.

The Masing manifold is a distinct concept from the Coulomb friction cone. Here, the Coulomb friction cone could be conceptualized as the stuck face (i.e., faces BDF or ACE) of the Masing manifold, and would indicate the set of all possible friction force vectors that can exist before slip. By contrast, the Masing manifold prescribes the hysteretic relationship for a friction element undergoing steady-state oscillation with, potentially, time varying normal force.

Because there are linear relationships between N, u, and f in each of the regions for an elastic dry friction model, the Masing manifold is able to be constructed using straight lines to connect the points identified above. If the relationship was nonlinear, then the connection between points would have to be modified accordingly. Likewise, there is also a piece-wise linear relationship between u and f. For hysteresis models that do not have linear or piece-wise linear relationships between u and f, it is expected that the Masing manifold would no longer be a prism, but rather a curved shape that reflects the transition from linear elastic behavior to macroslip (i.e., similar to the curves of Fig. 1). The present section has described how to construct a Masing manifold and the equations can be directly applied given a displacement history, thus the Masing manifold exists for any set of displacements.

From preliminary inspection of the Masing manifold, there are two special cases that must be considered for understanding if a frictional response with N varying would stay on the Masing manifold. Inspired by [43], different regimes of relative loading rates for the normal and tangential directions are considered. Both of these cases involve state changes for the friction model (i.e., when the model transitions from stick to slip and vice versa):

- If N decreases during the portion of the hysteresis loop before sliding begins (i.e., the stuck phase), then the threshold for sliding decreases and the transition from sticking to sliding needs to be assessed.
- If N increases during the sliding portion of the hysteresis loop (i.e., the slip phase), then the threshold for sliding increases and the transition from sliding to sticking needs to be assessed.

For the other scenarios (N increasing during the stuck phase or decreasing during the slipping phase), this does not result in a change in the state of the friction model, and thus stays on the Masing manifold by definition.

---

[1] In practice, this is able to be calculated more efficiently based off of the structure of the friction model. For elastic dry friction, analytical expressions for each of the surfaces of the Masing manifold are readily derived

[2] The displacement of the anchor corresponds to maximizing and minimizing Eqs. 3 and 4, respectively, which may be different than the maximum or minimum tangential displacements.

2.1 Normal Load Decreasing During the Stuck Phase

Upon the response entering the stuck phase, the equation of the friction force from elastic dry friction, before macroslip is achieved, is expressed in terms of the displacement u_0 and friction force f_0 at the start of sticking (lines BD and AC in Fig. 5)

$$f_{stuck} = k_T \left(u(t) - u_0\right) + f_0. \tag{7}$$

In terms of the Masing manifold, the stuck phase is described by responses that are on the triangles formed by either points ACE or BDF. If the response enters slip before passing zero tangential force, then the tangential force will be slipping opposite the velocity and thus not be on the manifold. This occurs when

$$f_{stuck}\text{sign}(u(t) - u_0) < -\mu N(t). \tag{8}$$

Physically, this constraint is interpreted as the spring in the elastic dry friction model relaxing as N is removed, allowing f to decrease as N decreases when the tangential displacement has not sufficiently unloaded the spring since load reversal. The constraint can be interpreted as limiting how fast, on average, N can decrease for any time period that starts when the slider first sticks and ends while the slider is still stuck with $f\text{sign}(u(t) - u_0) < 0$. Note that if N decreases to zero, the response will be on the manifold at that point since the slip force is equal regardless of sign or direction of motion.

Under constant N, the response enters the stuck face when the sign of the velocity changes. If N is increasing, then the response enters the stuck face when the velocity reverses *or* before, as addressed in the next section. Under decreasing N, the response will continue to slip on the same face while

$$\mu\frac{dN}{dt} \leq k_T\frac{du}{dt}\text{sign}(f) \leq 0, \tag{9}$$

corresponding to N decreasing more rapidly than the spring can elastically unload. The condition of Eq. 8 can only be applied once the response has entered the stuck face, not starting from the point of velocity reversal. Cases discussed in §3 illustrate the different distinctions.

2.2 Normal Load Increasing During the Slip Phase

Once the response transitions into slip, the second special case to consider is when N increases, thus also increasing the macroslip force μN. The potential concern is for N to increase faster than the linear elastic spring can stretch and thus the spring would be unable to maintain the slip condition of $f = \mu N$. Thus, as N increases, the stretching of the linear elastic spring must proportionally increase at the same rate to remain slipping; otherwise, the system will transition to the stuck state, which would manifest as the trajectory leaving the manifold. This establishes a second constraint for remaining on the manifold: N cannot increase faster than $k_T u_{rel}$ (where u_{rel} is the stretching of the linear elastic spring). Since the spring is linear, the slipping regime must maintain that

$$\mu N(t)\text{sign}(u_{rel}) = k_T u_{rel}(t) \tag{10}$$

for

$$u_{rel} = u(t) - u_{anchor}(t). \tag{11}$$

The quantity $u(t) - u_0$ is inappropriate here once the system starts slipping, so the displacement of the spring is calculated based on the position of the anchor. The constraint on the rate of change of N (and u_{rel}) in the slipping regime thus becomes

$$\mu\frac{\mathrm{d}N}{\mathrm{d}t} = k_T\frac{\mathrm{d}u_{rel}}{\mathrm{d}t}\text{sign}\left(u_{rel}\right) = k_T\left[\frac{\mathrm{d}u(t)}{\mathrm{d}t} - \frac{\mathrm{d}u_{anchor}(t)}{\mathrm{d}t}\right]\text{sign}\left(u_{rel}\right). \tag{12}$$

Here, it is noted that on the manifold,

$$\text{sign}(f) = \text{sign}(u(t) - u_0) = \text{sign}(u_{rel}(t)) \tag{13}$$

for the slipping regime, since N is increasing. Based on the anchor interpretation of the friction model when N is increasing,

$$\text{sign}\left[\frac{\mathrm{d}u_{anchor}(t)}{\mathrm{d}t}\right] = \begin{cases}\text{sign}(f) & Slipping\\ 0 & Stuck.\end{cases} \tag{14}$$

Therefore,

$$\frac{\mathrm{d}u_{anchor}(t)}{\mathrm{d}t}\operatorname{sign}\left(u_{rel}(t)\right) \geq 0, \tag{15}$$

leading to the constraint

$$\mu\frac{\mathrm{d}N}{\mathrm{d}t} \leq k_T\frac{\mathrm{d}u}{\mathrm{d}t}\operatorname{sign}\left(u(t)-u_0\right). \tag{16}$$

One interpretation is that these two constraints (Eqs. 8 and 16) impose a limit on the rate of change[3] for N if the hysteretic response of the system is to stay on the Masing manifold. A second interpretation is that these constraints establish the limits for how u must change in the presence of a time varying N.

In some cases, a violation of Eq. 16 corresponds to the system entering the stuck phase rather than the response leaving the manifold. Specifically, if Eq. 16 is violated at time t_1 and the velocity changes sign at t_2, then the response will stay on the manifold if

$$k_T(u(t)-u(t_1)) + f(t_1) \leq \mu N(t) \quad \forall t \in [t_1, t_2]. \tag{17}$$

This is physically interpreted as the response entering the stuck face at t_1 and staying stuck until at least the velocity reverses. Examples violating Eq. 16, which correspond to leaving the manifold or entering the stuck phase before velocity reversal, are shown in §3.

2.3 The Degenerate Case of No Hysteresis

For hysteretic models that remain in the linear elastic portion of the response (i.e., when Eq. 1 simplifies to $f = k_T u(t)$ for all u in the response, which is the case of hysteresis loops B and E in Fig. 2), the Masing manifold condenses to a two-dimensional triangle in the displacement-hysteresis force-normal force space. This is captured by the anchor remaining fixed in one place and the second case of Eq. 5. Even with N changing, the response can still conform to the Masing manifold provided that $|k_T u(t)| \leq \mu N$, as will be observed in §4. If N decreases such that $|k_T u(t)| > \mu N$, this would mark the inception of slip and would no longer qualify as a degenerate case. As such, the full Masing manifold should be used instead.

2.4 Uniqueness of Masing Manifold

For a given periodic displacement history, the Masing manifold is uniquely defined in § 2. However, under some conditions alternative manifolds exist. First, the case where slip occurs in the steady-state response is considered. Any manifold to describe the true frictional force should match the proportional slip limit planes of $f = \mu N$. Therefore, the manifold is unique if and only if the stuck planes are uniquely defined. Under the conditions defined in § 2.1 and § 2.2, there are two unique regions where the slider is stuck in the truth friction model defined by Eq. 1. Within a given stuck regime, if a single point is matched by the manifold, the entire stuck regime is matched by the manifold since the manifold captures the tangential stiffness correctly and there is no relationship other than Eq. 6 that would capture the tangential stiffness. Therefore, the manifold is unique and matches the friction force if the calculation of $u_{anchor,amp}$ is unique and matches the friction evaluations.

With regards to the stuck planes, the contact is in the stuck state when the velocity of the anchor is zero, which only occurs during the two transitions from slipping in the positive and negative directions given that the conditions defined in § 2.1 and § 2.2 are met. During this transition, the anchor must be in the extreme maximum and minimum locations since it is the reversal of the direction of the anchor. The extrema of the anchor positions correspond to the calculations given by Eqs. 3 and 4. These extrema correspond to maximizing (or minimizing, respectively) Eq. (2) under the conditions of positive (negative) slipping forces corresponding to reversal from positive to negative (negative to positive) slipping direction. Eq. (2) is derived by rearranging the expression for the history variables in stuck regime and thus results in the manifold matching the full stuck regime. As long as the normal force is greater than zero at the reversal of the anchor, then a finite time period is required for the spring to unload and reload in the opposite direction. Thus the friction force is evaluated in the stuck regime and the stuck plane must be defined to match the frictional evaluation as is done in the present construction.

---

[3] While Eq. 8 does not impose a limit on the differential rate of change of N at a specific time, it can be interpreted as placing limits on the average rate of change.

If there is no contact when the velocity reverses (i.e., $N = 0$), then the frictional response immediately goes from one slipping face to the slipping face for the opposite direction. In this case, the stuck plane does not need to be defined for the manifold to match the frictional force. Therefore, there is not a unique definition of the Masing manifold when the reversal occurs while the contact is separated. Rather for transition from positive to negative (respectively negative to positive) velocity, any value of $u_{max,anchor}$ greater ($u_{min,anchor}$ less) than the value given by Eq. (3) (Eq. (4)) is valid. The construction defined in § 2 generates a unique manifold by choosing the smallest possible slip region planes in this case.

The next situaiton to consider is the case where the steady-state response includes slipping, but the conditions of § 2.1 and § 2.2 are not satisfied. Here, one could define different Masing manifolds using different stuck regimes (e.g., before versus after the condition is violated). In that case, each manifold would exactly match the frictional response over different regimes, and the manifold would not be unique. Throughout the rest of this paper, the construction presented in § 2 is used to select a single manifold when the conditions of § 2.1 and § 2.2 are not satisfied.

In the degenerate case, the manifold is not uniquely defined because multiple different history variables could result in frictional forces in the stuck regime for all time. In simulations, this issue is not unique to the Masing manifold, but rather inherent to the friction model. One can add additional constraints to make the friction evaluations unique. Such additional constraints can be applied either to the Masing manifold or the original friction evaluations from Eq. 1. The previous construction yields a unique Masing manifold for the degenerate case, but the equations could be altered to give a different valid manifold.

3 Demonstration on a Simple Harmonic Oscillator

To test the Masing manifold hypothesis, a simple harmonic oscillator is first considered. In the following simulations, a single degree of freedom mass spring oscillator is studied with prescribed displacement ($u = 50 \sin(2\pi t)$ nm). The oscillator is in frictional contact with ground via an elastic dry friction element (Eq. 1). Using the properties[4] $\mu = 0.9627$ and $k_T = 5.26 \times 10^{14}$ N/m, the Masing manifold is constructed using the procedure outlined above, and the hysteretic response is calculated for a number of different functions describing N. With the responses shown in Fig. 6, these include a constant normal force ($N = 5$ MN, Fig. 6(a)-(b)), and sinusoidally varying normal forces of $N = 2.5 \sin(2\pi t) + 5$ MN (Fig. 6(c)-(d)), $N = 2.5 \sin(2\pi t - \pi/4) + 5$ MN (Fig. 6(e)-(f)), and $N = \max(0, 2.5 \sin(4\pi t) + 1)$ MN (Fig. 6(g)-(h)).

The hysteresis loops shown in Fig. 6(a), (c), (e), and (g) each fall upon the corresponding Masing manifolds exactly. Only the case of constant N conforms to the original Masing conditions, while the second and third cases are clearly asymmetric. As the form for $N(t)$ becomes more complicated, the deviation of the hysteresis loops from the one formed by the traditional Masing conditions (i.e., $N = 5$, Fig. 6(a)-(b)) increases; however, each of the four hysteresis loops still conform to the Masing manifold. For the response in Fig. 6(e) and (f), the transition from positive velocity to negative velocity occurs *after* the transition from slipping to sticking. This is manifested on the Masing manifold as the response lying on the line between the slip face and stuck face until the velocity changes direction, at which time it transitions to the stuck face, and is further highlighted in Fig. 7. This behavior occurs since N increases too quickly near the reversal point, violating the condition of Eq. 16, but still satisfies Eq. 17, resulting in it remaining on the manifold. In the fourth case (Fig. 6(g) and (h)), the velocity changes sign before the response leaves the slip face. This occurs because N decreases too quickly near the reversal point and results in reverse slipping as discussed in §2.1. However, since this occurs continuously at the reversal point and satisfies Eq. 9, the response does not leave the manifold. Consequently, none of these examples violate the constraint conditions of §2.

3.1 Violations of the Constraint Conditions

In order to investigate regimes where the constraint conditions of §2 are clearly violated, resulting in a significant deviation between the Masing manifold and the actual hysteresis loop, two further examples in which N suddenly increases and decreases during the steady-state oscillation are investigated. For the first example, N is modeled as

$$N(t) = 2 \times 10^6 + 3 \times 10^6 \left(H(t - 0.5)\right) \left(1 - H(t - 0.6)\right) \left(1 - \cos^2\left(\frac{2\pi}{0.2}(t - 0.5)\right)\right), \tag{18}$$

using the Heaviside step function $H(\tau)$, which is defined as 0 for $\tau < 0$ and 1 otherwise, and is plotted in Fig. 8(a). As shown in Fig. 9(a) and (b), the rate of change of N is sufficiently high that the constraint condition is violated and the hysteresis no longer conforms to the Masing manifold. The response is shown to penetrate the Masing

---

[4] These values are chosen for consistency with the next section.

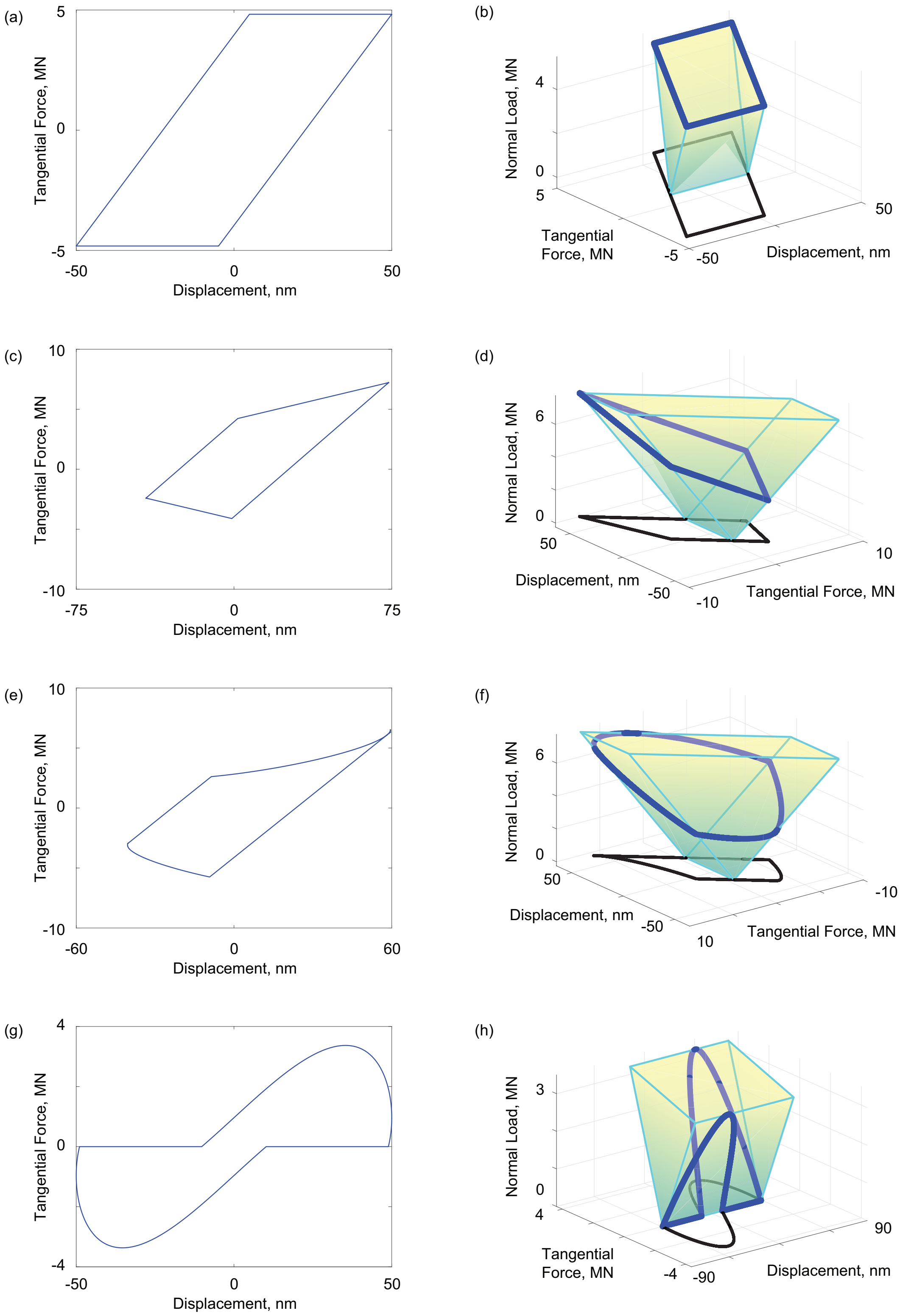

Fig. 6: Hysteresis loops and Masing manifolds for (a)-(b) constant normal force, (c)-(d) sinusoidally varying normal force in phase with the displacement, (e)-(f) sinusoidally varying normal force that is $\pi/4$ rad out of phase with the displacement, and (g)-(h) sinusoidally varying normal force that goes to zero. All results are from the elastic dry friction model. The black curves on the right plots are the projections of the hysteresis loops onto the $N = 0$ plane for visualization purposes.

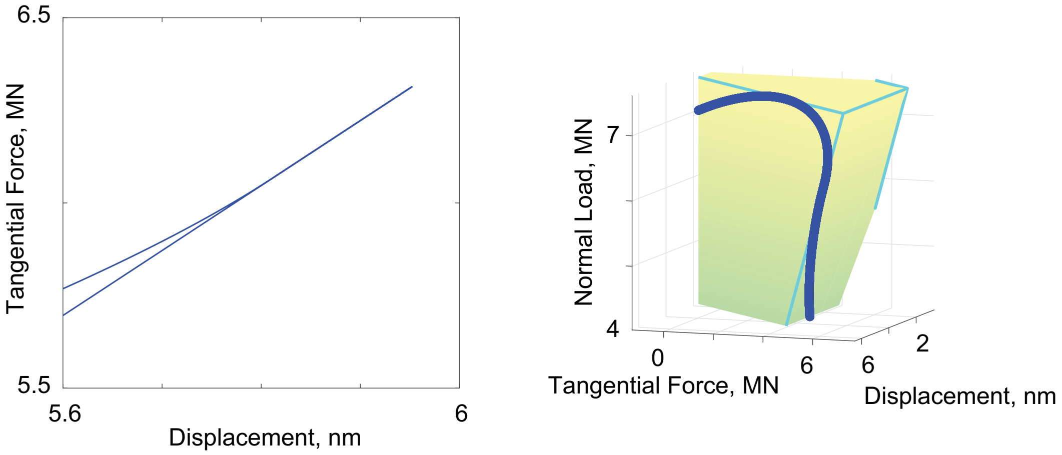

Fig. 7: Highlight of the third case (a sinusoidally varying N, shown in Fig. 6(e)-(f)), showing zoomed in views of the hysteresis loop (left) and Masing manifold (right).

manifold in Fig. 9(b); whereas, if the response was constrained to lie on the Masing manifold, the red curve would be generated instead. As discussed in §2, one interpretation of the constraint is that it relates how quickly f must change as N changes. Here, the tangential stiffness limits the rate of increase of f with changes in N, and as such the true response of f is lower in magnitude than if f was constrained to stay on the Masing manifold (i.e., the red curves in Fig. 9).

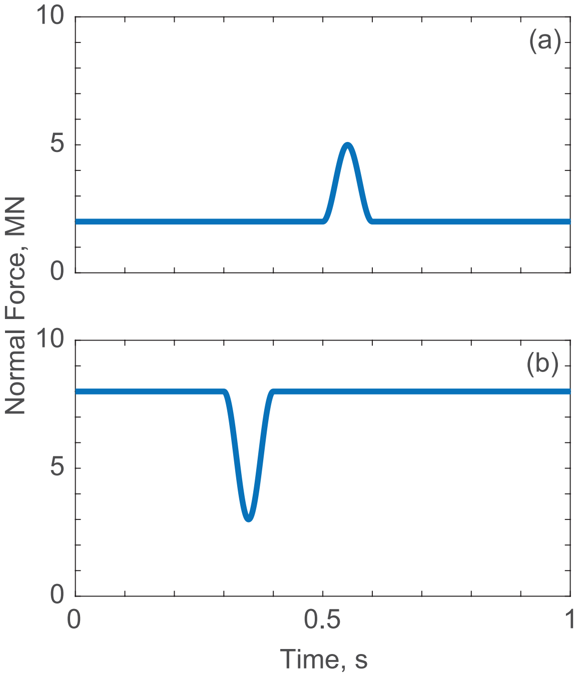

Fig. 8: Normal force as a function of time for the violation examples, showing (a) Eq. 18 and (b) Eq. 19.

The second type of violation, discussed in §2.1, requires a sudden decrease in N while in the stuck regime. To investigate this violation, after velocity reversal while the response at constant N would be in the stuck regime, an impulse is applied to the system. In this case, N is modeled as

$$N(t) = 8 \times 10^6 - 5 \times 10^6 \left(H(t-0.3)\right)\left(1 - H(t-0.4)\right)\left(\sin^2\left(\frac{2\pi}{0.2}(t-0.3)\right)\right), \tag{19}$$

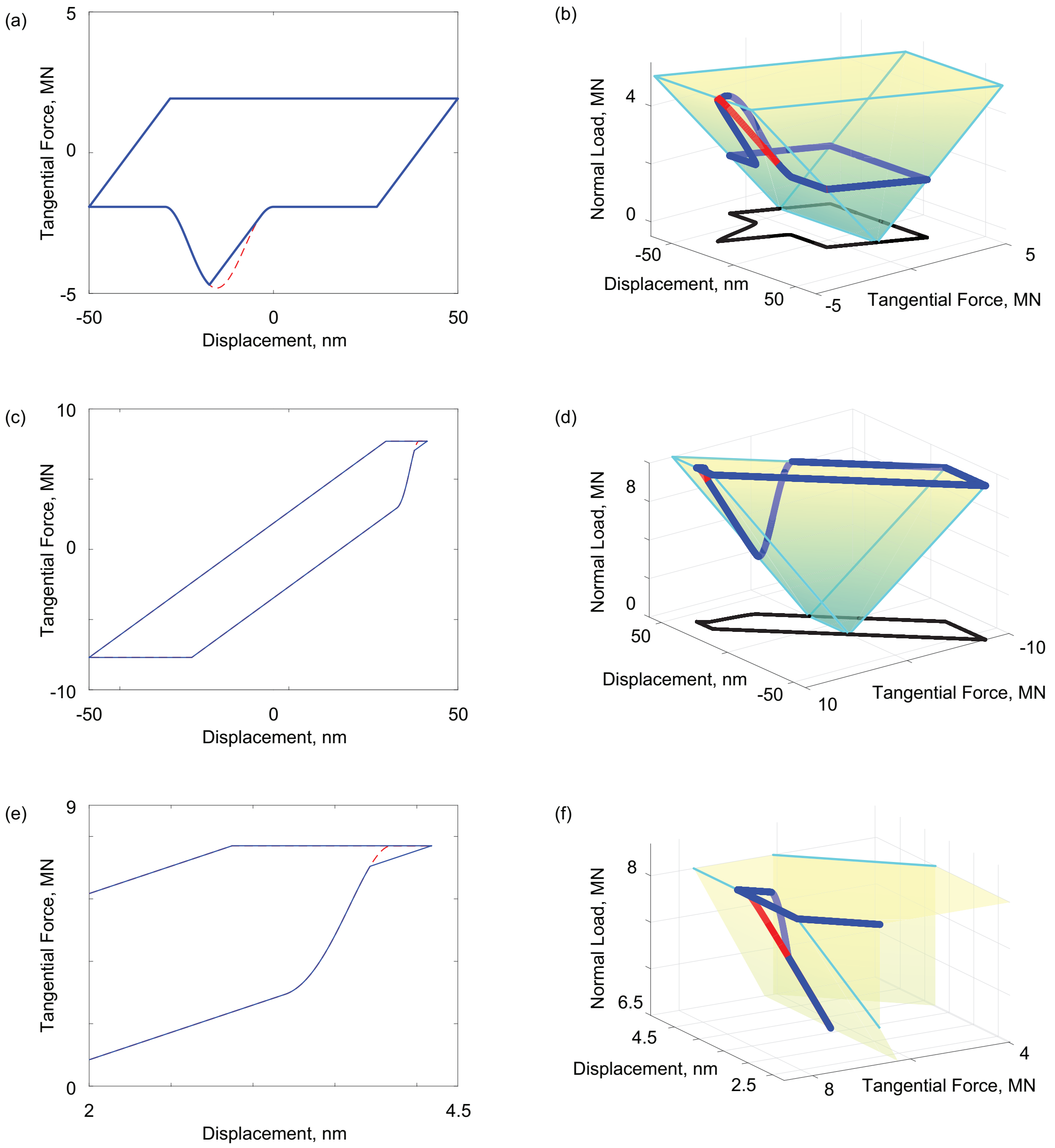

Fig. 9: Hysteresis loops (left) and Masing manifolds (right) for normal loads that violate the constraint conditions laid out in §2, with N described by Eq. 18 in (a) and (b), and Eq. 19 in (c)-(f) (with (e) and (f) being a zoomed in highlight to better show the violation). The blue curves indicate the true tangential forces, the red curves indicate the tangential forces if they are constrained to stay on the Masing manifolds, and the black curves in the right subplots are the true tangential forces projected onto the $N = 0$ plane.

which is plotted in Fig. 8(b). The true response starts to unload elastically and penetrate the manifold from 0.3 to 0.35 s (with a small drop in f) before the large drop in f that returns it to the manifold surface is observed; the manifold response, by contrast, maintains a constant f as u decreases before the large drop in f is observed, as shown in Fig. 9(c)-(f). When N decreases, both the manifold response and the true response decrease rapidly on the slip face before eventually following the stuck phase. Thus, violations of the conditions set forth in §2 will result in the Masing manifold deviating from the actual hysteresis of the system.

4 Applicability to Built-Up Structures

In order to assess the applicability of the Masing manifold to multi-degree of freedom systems (in particular, jointed structures), the steady-state response of the Brake-Reuß beam [3], the geometry of which is shown in Fig. 10, is studied. The Brake-Reuß beam, which is a prismatic beam with a three-bolt lap joint, is modeled using a tribomechadynamic modeling approach that is described in detail in [19, 21, 37] and briefly summarized here.

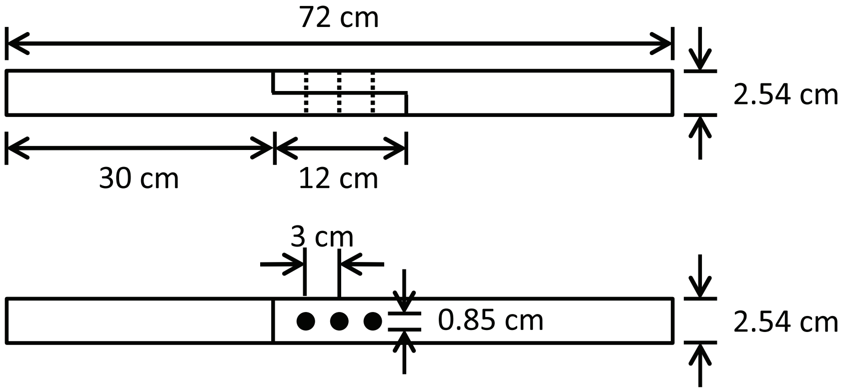

Fig. 10: Geometry of the Brake-Reuß beam [3].

4.1 System Model

The initial finite element model of the Brake-Reuß beam is first reduced with a Hurty/Craig Bampton Component Mode Synthesis [44, 45] to the interface degrees of freedom plus 19 additional fixed interface modes. The resulting model is then further reduced to the final 122 zero thickness elements (ZTEs) with 156 nodes (each with three translational degrees of freedom (DOFs)) [21]. The ZTEs are used to model the interface accurately in a hyper-reduced framework[5] that facilitates implementation of different friction and wear models [37] and simplifies calculations by eliminating the need for contact searches. The mesh of the ZTEs is superimposed on top of the original mesh of the interface, and is shown in the center of Fig. 2. Six of the original 19 fixed interface modes correspond to rigid body modes and are eliminated at the second reduction [19], leaving 13 fixed interface modes in the final ROM.

The response of the Brake-Reuß beam to steady-state excitation is simulated using the extended periodic motion concept (EPMC) [28]. EPMC solves for a periodic modal response (parameterized with both the zeroth order and the first three harmonic coefficients of each DOF), a mass proportional forcing amount (applied by EPMC in order to balance the damping in the nonconservative system), and a modal frequency. For the EPMC simulations, mass and frequency proportional damping are applied to the model to yield modal damping levels of 8.7e-4 and 3.4e-2 for the first two bending modes of the linearized system, respectively, in order to match the low amplitude experimentally measured damping of the system. Such damping is necessary since friction models are generally unable to reproduce low amplitude damping [37, 22], which is generally referred to as material damping.

The nonlinear forces are evaluated in the time domain with the alternating frequency-time (AFT) approach [46, 47, 48]. For the AFT scheme, harmonic coefficients are converted to time domain displacements at the nonlinear DOFs. Frictional tractions are then evaluated in the time domain using an elastic dry friction model described both with a Masing manifold (following the procedure of §2; only one Masing manifold is calculated for all ZTEs, with the frictional response of each ZTE being determined by that specific element's t_n and u_q) and directly without any assumptions related to the Masing conditions. The Fourier transform of the forces in the time domain is evaluated to apply the forces in the frequency domain. The forces in the time domain are evaluated for 128 equally spaced time intervals of length Δt over the interval $[0, T - \Delta t]$ for a fundamental period of T. If the given DOF slips, the friction forces are evaluated for two cycles to converge the hysteresis loops, and the Fourier transform of only the second cycle is evaluated.

The elastic dry friction model uses a penalty normal contact model with zero normal tractions when the interface is separated. For a given normal displacement u_n, the normal traction t_n is

$$t_n = \begin{cases} k_n u_n(t) & u_n(t) > 0 \, (contact) \\ 0 & Otherwise \, (separation), \end{cases} \tag{20}$$

where k_n is the normal stiffness of the contact. The tangential tractions are parameterized by a tangential stiffness k_t as well as μ (note that since the model is formulated using tractions, k_t has units of N/m^3). The tangential traction t_q

---

[5] Here, hyper-reduced refers to a ROM in which no transformation between reduced and full coordinates is needed in order to evaluate the interfacial forces at each step of the simulation.

generated by a tangential displacement u_q is

$$t_q = \begin{cases} \underbrace{k_t(u_q(t) - u_{q,0}) + t_{q,0}}_{t_{stuck}} & |t_{stuck}| < \mu t_n(t) \\ \mu t_n(t)\text{sign}(t_{stuck}) & \text{Otherwise.} \end{cases} \tag{21}$$

Here, $u_{q,0}$ and $t_{q,0}$ are the displacement and tangential traction respectively at the previous instant and q can denote either the x or y tangential direction. Equation 21 is equivalent to Eq. 1 except that it is formulated in terms of tractions instead of forces. Following the procedure of §2, a Masing manifold for this friction model is constructed *a prior* for use in the simulations. As the interface is considered two-dimensional, the friction model (Eq. 21) is applied independently in the x and y directions. While this is not completely physical, this decoupling significantly reduces the computation complexity of the gradients for the solution and has minimal effect on the overall dynamics of the structure given the primary direction of motion is aligned with the xy-coordinate system of the mesh [22].

The parameters for the elastic dry friction model are curve-fit to the experimental results reported in [37], yielding $\mu = 0.9627$, $k_t = 5.261 \times 10^{14}$ N/m^3, and $k_n = 5.765 \times 10^{11}$ N/m^3. The resulting amplitude-dependent frequency and damping of the first bending mode are shown in Fig. 11. A relatively large response amplitude is chosen for what follows in order to investigate highly dissipative responses that would best test the validity of the Masing manifold hypothesis. The hysteresis loops of several points along the interface at the amplitude indicated in Fig. 11 are shown in Fig. 2.

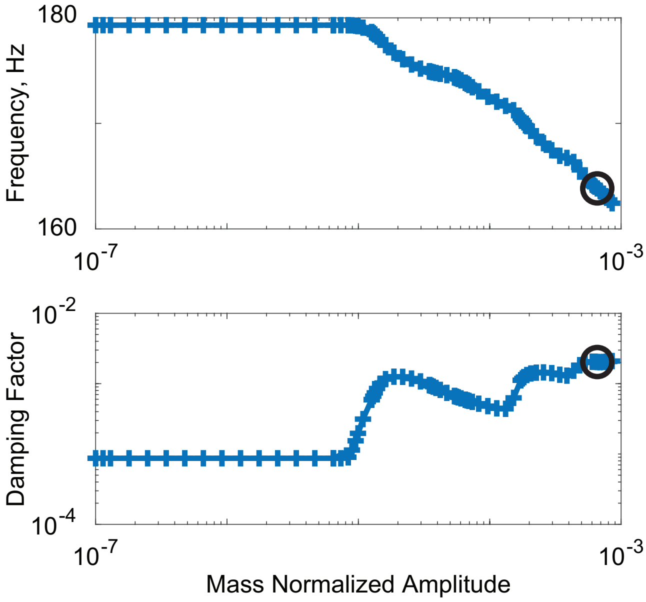

Fig. 11: System level response of the Brake-Reuß beam, in terms of frequency and damping factor of the first bending mode, as a function of mass normalized response amplitude. Black circles indicate the amplitude at which the hysteresis curves are reported.

4.2 Hysteretic Responses

Each ZTE included in the Brake-Reuß beam ROM has its own hysteretic response. Six of these responses are shown in Fig. 2, and are further investigated here. These responses are chosen because they represent the variety of hysteretic responses observed across all elements. As the responses of the outermost elements (e.g., A and F in Fig. 2) shown are similar, only one is detailed in what follows. Likewise, as most of the inner elements exhibit linear elastic responses (e.g., B and E in Fig. 2), only one is discussed below as well.

The outermost elements (e.g., A and F in Fig. 2) experience a clapping response in which the surfaces come in and out of contact periodically. The Masing manifold for hysteresis loop F of Fig. 2 is shown in Fig. 12. As t_n goes to zero, the response on the Masing manifold traces to the line in u_q for $(t_q, t_n) = (0, 0)$[6]. At the load reversal (near

---

[6] Recall, t_q is the tangential traction that is related to f, and t_n is the normal traction that is related to N.

a normalized time of 0.35), the sudden increase of frictional traction is due to movement across the stuck face (as $k_t = 5.261 \times 10^{14}$ N/m^3, large tractions result for small displacements). The reduction in the magnitude of t_q just before the load reversal (near a normalized time of 0.25) is due to t_n decreasing while the slider is still in the slip regime. Throughout all of these dynamic events, the hysteretic response stays on the Masing manifold exactly.

One row of elements more internal to the interface, such as element D (from Fig. 2), experience t_n that approach, but do not achieve, a value of zero, as shown in Fig. 13. At both load reversals, there is a significant change in t_q; however, for the first load reversal (near a normalized time of 0.28), the change in t_q is significantly smaller as t_n is close to zero at this point. The change in slope of t_q just before the load reversal is due to t_n changing from decreasing to increasing again just before the friction model begins to unload. At the second load reversal, near a normalized time of 0.93, t_n is near its maximum resulting in a significantly larger change in t_q as the friction model transitions from sliding before the load reversal, to stuck immediately after, then to sliding shortly later. An important observation for element D is that even though u_q is not sinusoidal (and is multi-harmonic), the loading portion of the response is monotonically increasing in u_q and the unloading portion of the response is monotonically decreasing in u_q. Thus, even though the response is not sinusoidal, because it is monotonically increasing then monotonically decreasing, the fundamental assumption of the Masing conditions is not violated (i.e., that the response oscillates between two extrema).

Most of the internal elements exhibit linear elastic responses as they never progress out of the stuck state, such as elements B and E in Fig. 2. The Masing manifold for element E is presented in Fig. 14. As the hysteresis loop is degenerate (i.e., exhibits no hysteresis), the Masing manifold is compressed into a two-dimensional triangle. As t_n and u_q vary, t_q is constrained such that the response curve is exactly on the Masing manifold. Similar to element D, the response has slight contributions from higher harmonics; however, the loading portion is strictly monotonically increasing in u_q and the unloading portion is strictly monotonically decreasing in u_q.

As a last example, element C from Fig. 2 is an internal element that exhibits dissipative behavior. The Masing manifold for element C is shown in Fig. 15. Due to the high value of t_n and relatively large changes in u_q (compared to element E, Fig. 14), the element exhibits both stuck and slipping behavior. As with all of the other elements within the interface, this hysteretic response of this element exactly conforms to the Masing manifold.

4.3 Accuracy and Computational Time

The hysteretic responses of Figs. 12-15 are calculated with two different approaches: using the present Masing manifold approach and using the traditional approach of representing friction via Eq. 21 without any assumptions related to the Masing conditions. In the first approach, the Masing manifolds are calculated *a priori*, as descried in §4.1. For the second approach, the response is post-processed to determine if it falls upon the Masing manifold. No differences are able to be observed between the two methods. This gives confidence that friction can be represented accurately with a Masing manifold, provided that none of the fundamental constraints discussed in §2 are violated.

The use of Masing manifolds offers a tremendous opportunity to reduce computational time, much like the original Masing conditions did. While the present simulations were not developed to consider computational time, several observations can still be made. First, the results presented in §3 were found analytically; no direct time integration was needed. Comparison of computational time for this example thus has little value due to the simplicity of the system not requiring a simulation. For the results presented in §4, numerical simulations were necessitated to calculate the dynamic response of the structure. The representation of the friction elements, however, was found analytically instead of through a series of differential or integral equations. With the current implementation of the Masing manifolds, only a modest improvement of computational time was demonstrated (approximately a 10% reduction) as optimizing the code for efficiency was not the focus of the present research. In ongoing work, though, it is possible to incorporate Masing manifolds into harmonic balance simulations such that the alternating time frequency analysis may be by-passed in favor of a purely frequency domain computation (with the nonlinear hysteresis forces being analytically evaluated via the Masing manifold), resulting in a computational savings of up to 50%. Thus, this promises a new approach for the treatment of nonlinear forces in harmonic balance calculations, and is the subject of subsequent investigations.

5 Conclusions

Based on the work shown here, in which the fundamental hypothesis relating the Masing conditions to the normal force cannot be rejected, a revision to the Masing conditions, collectively referred to as the Masing manifold, is proposed. For the steady-state oscillation of a system between two extrema, the resulting hysteretic behavior is described by the manifold in the tangential displacement-tangential force-normal force space constructed according

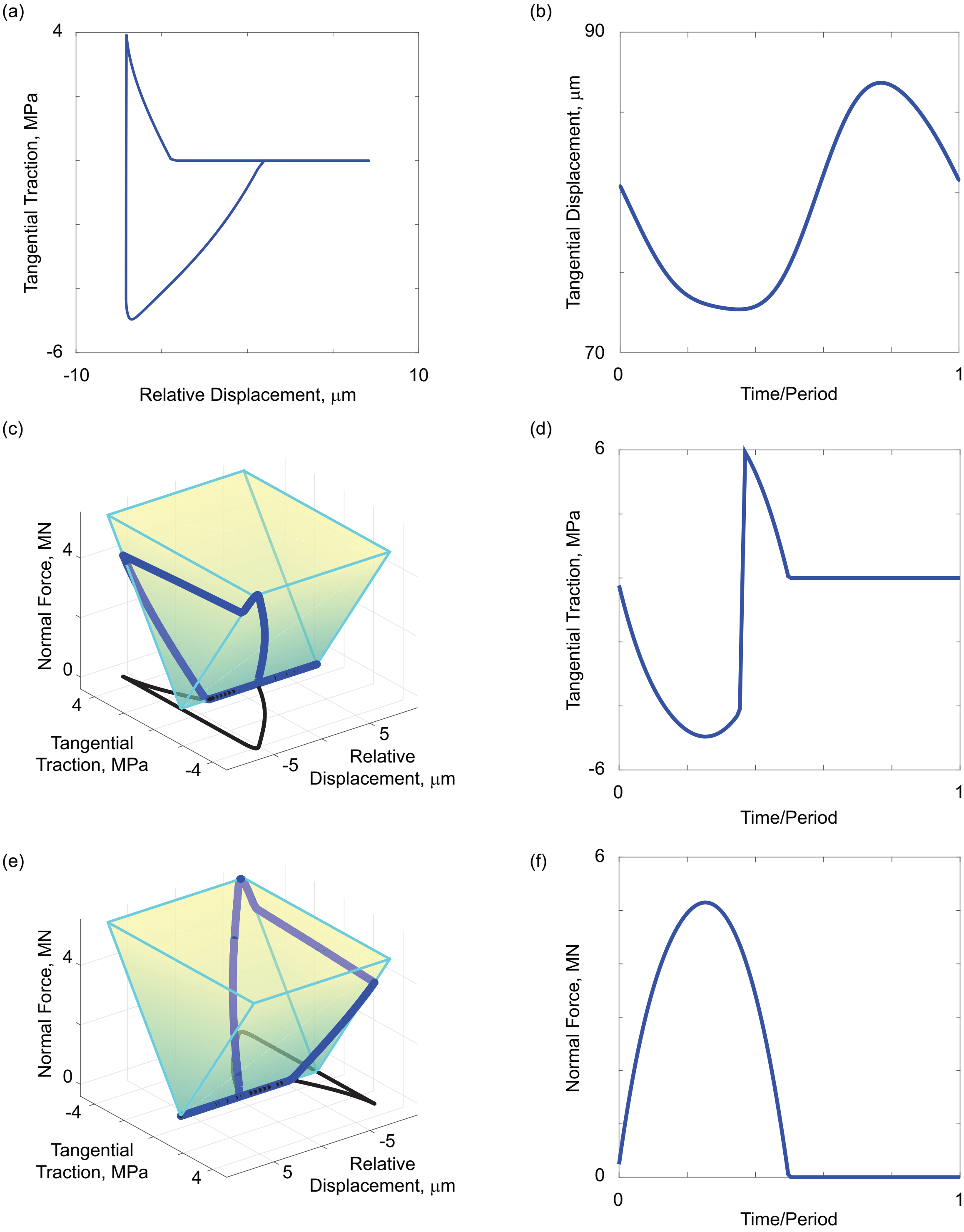

Fig. 12: Hysteretic response of element F (as indicated in Fig. 2) of the Brake-Reuß beam showing the (a) hysteresis loop, (b) original displacement as a function of time normalized by the period of the response, (c) Masing manifold in the displacement-traction-normal force space, (d) traction as a function of normalized time, (e) view of the Masing manifold rotated 180° about the t_n axis, and (f) normal force as a function of normalized time. For the Masing manifolds, the traction-displacement response is projected on the $t_n = 0$ plane as a black line. The response itself is indicated as the blue loop.

to the method established in §2. In short, the Masing manifold is the locus of points generated by independently constructing hysteresis loops across a range of normal forces, resulting in a three-dimensional manifold in the

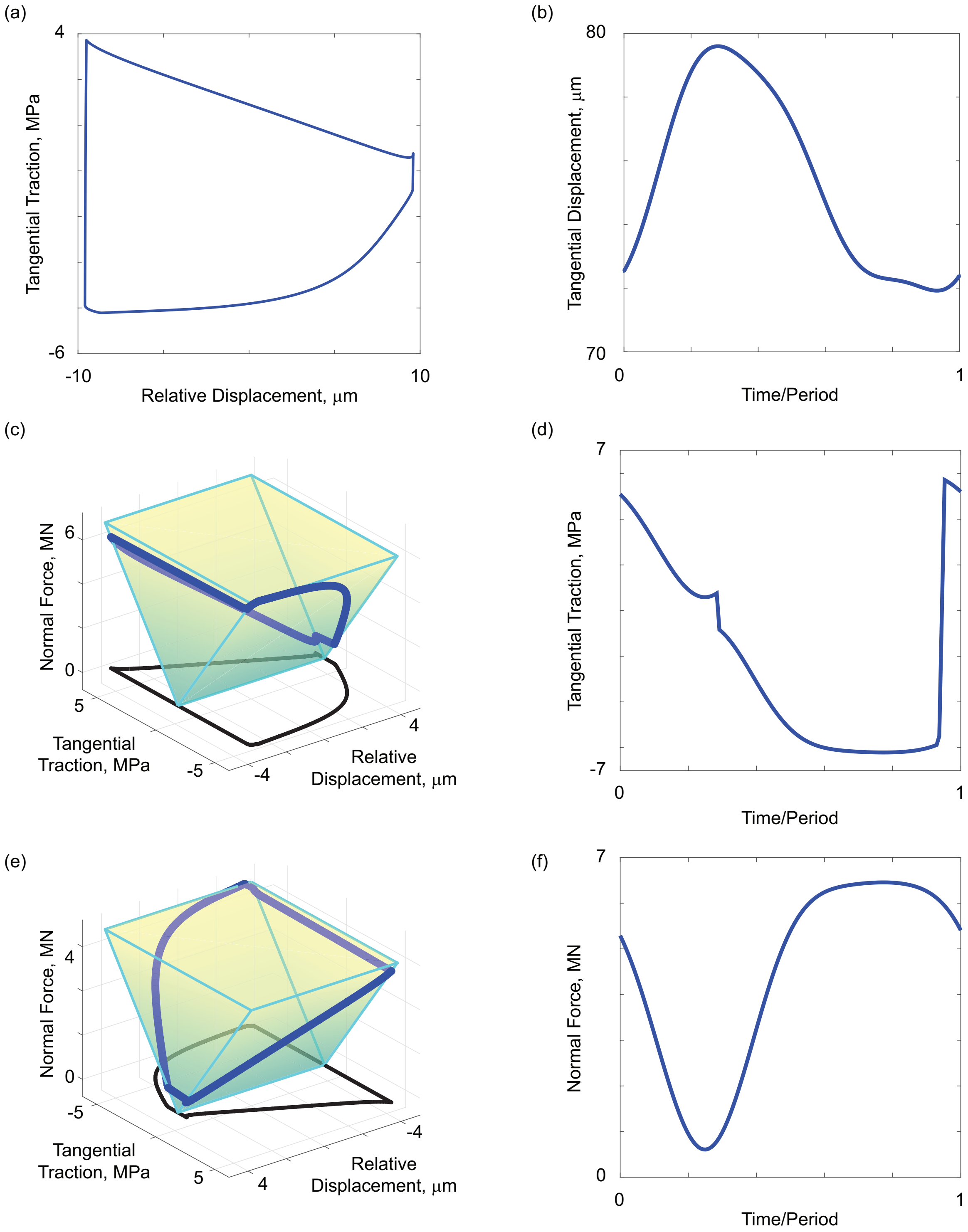

Fig. 13: Hysteretic response of element D (as indicated in Fig. 2) of the Brake-Reuß beam showing the (a) hysteresis loop, (b) original displacement as a function of time normalized by the period of the response, (c) Masing manifold in the displacement-traction-normal force space, (d) traction as a function of normalized time, (e) view of the Masing manifold rotated 180° about the t_n axis, and (f) normal force as a function of normalized time. For the Masing manifolds, the traction-displacement response is projected on the $t_n = 0$ plane as a black line. The response itself is indicated as the blue loop.

tangential displacement-tangential force-normal force space. Whether a response conforms to the manifold is subject to a condition imposed on the rate of change of the normal force relative to the tangential displacement.

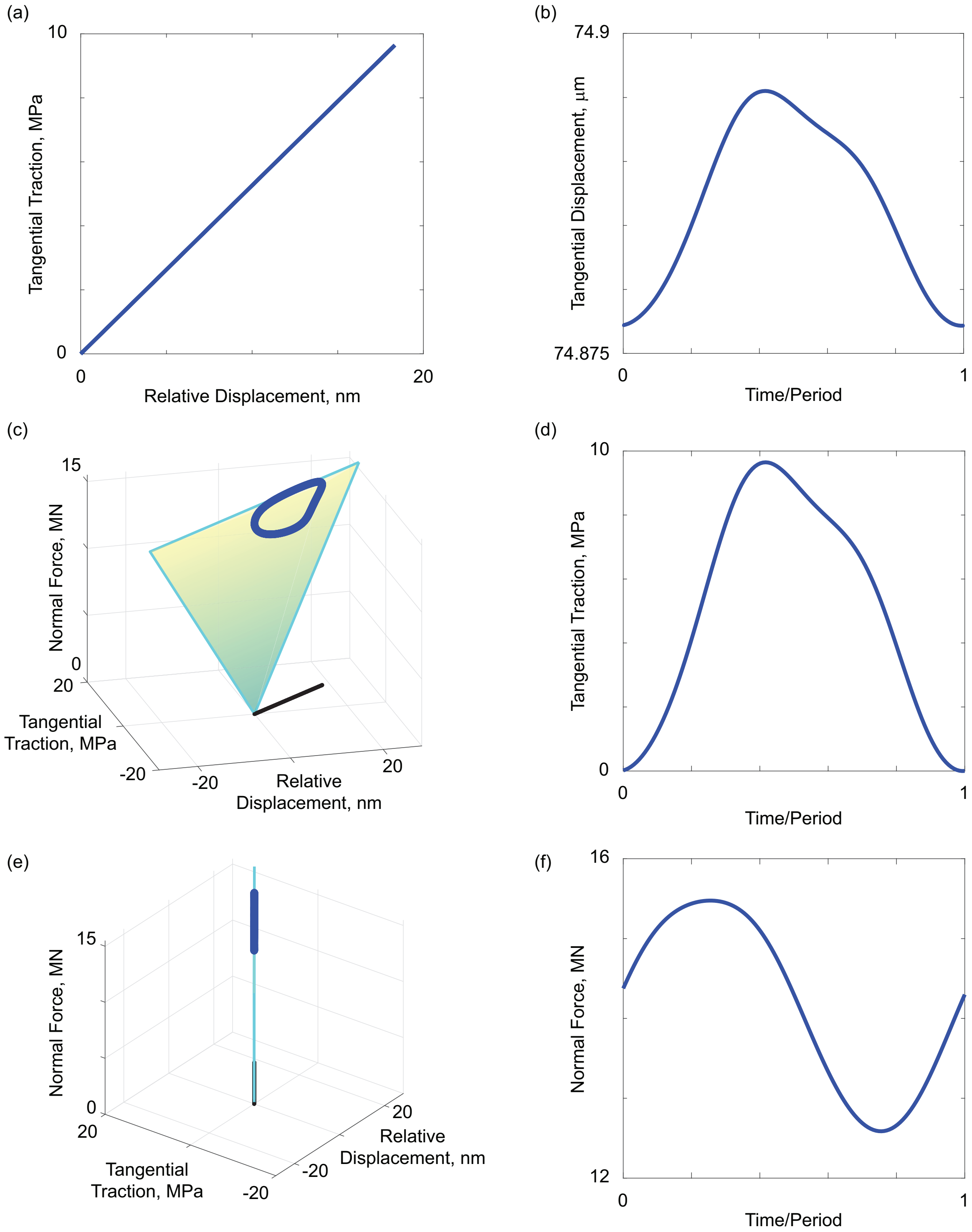

Fig. 14: Hysteretic response of element E (as indicated in Fig. 2) of the Brake-Reuß beam showing the (a) hysteresis loop, (b) original displacement as a function of time normalized by the period of the response, (c) Masing manifold in the displacement-traction-normal force space, (d) traction as a function of normalized time, (e) view of the Masing manifold aligned to show that the response never deviates from it, and (f) normal force as a function of normalized time. For the Masing manifolds, the traction-displacement response is projected on the $t_n = 0$ plane as a black line. The response itself is indicated as the blue loop.

The Masing manifold concept has been demonstrated here both for a simple harmonic oscillator as well as a built-up structure with hundreds of degrees of freedom and many discrete hysteretic elements, showing its effectiveness

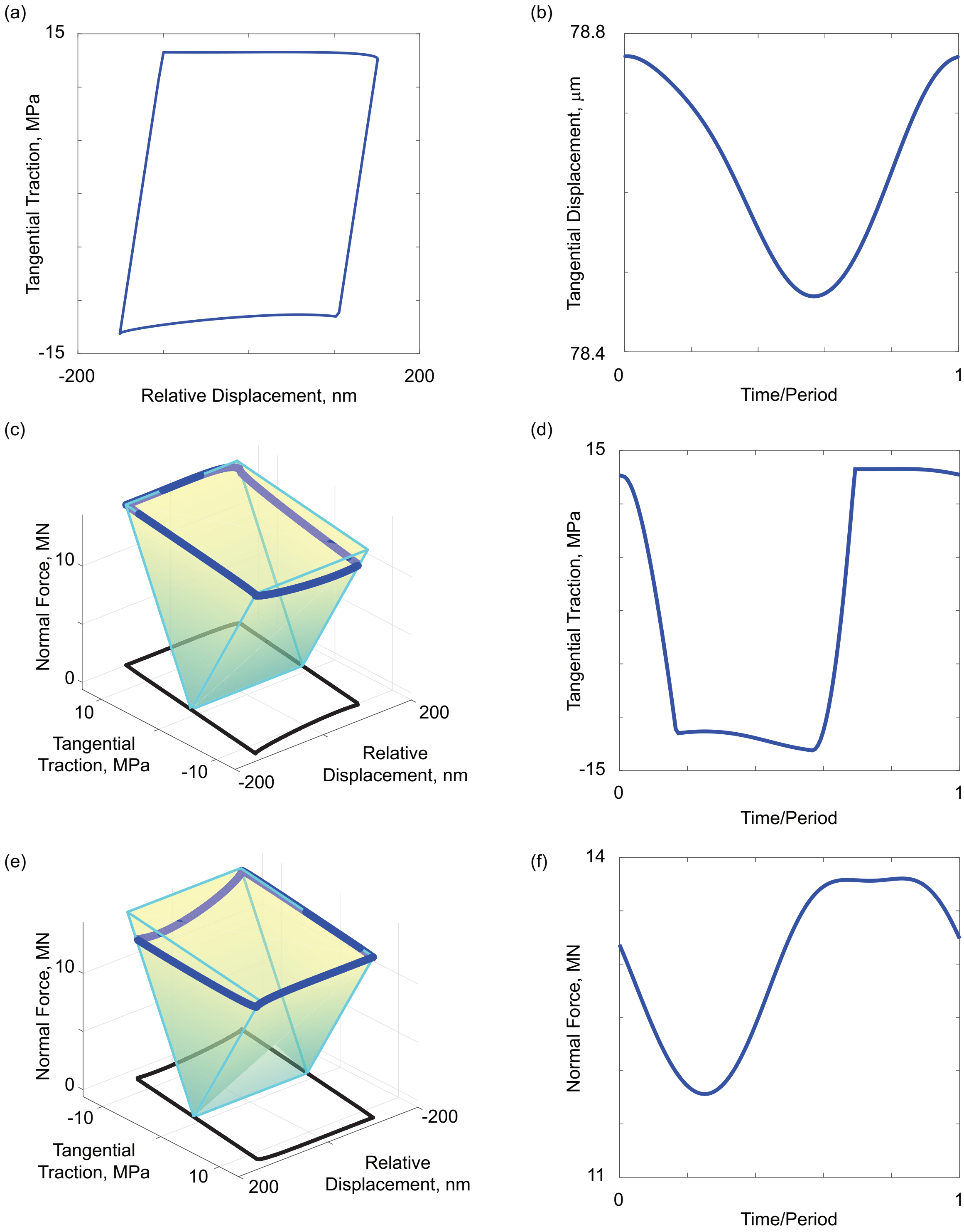

Fig. 15: Hysteretic response of element C (as indicated in Fig. 2) of the Brake-Reuß beam showing the (a) hysteresis loop, (b) original displacement as a function of time normalized by the period of the response, (c) Masing manifold in the displacement-traction-normal force space, (d) traction as a function of normalized time, (e) view of the Masing manifold rotated 180° about the t_n axis, and (f) normal force as a function of normalized time. For the Masing manifolds, the traction-displacement response is projected on the $t_n = 0$ plane as a black line. The response itself is indicated as the blue loop.

to represent hysteresis in jointed structures more realistically than the original Masing conditions. As this work has focused on the simple, elastic dry friction hysteresis model, it must next be generalized to other friction models. Thus, future work must seek to assess the validity of the Masing manifold for studying more complex hysteresis models (such as normal force dependent Iwan models). Not investigated here is whether the concept of a Masing manifold can be applied to non-Masing hysteretic models (such as a general Bouc-Wen model). It is expected that the Masing manifold concept can be applied to other Masing models, such as the four parameter Iwan model [39]; however, the generalizability of the concept is unknown.

The concept of the Masing manifold has several significant consequences. First, because it establishes a constraint relationship for how the tangential force must behave for a given displacement and normal load, it negates the need for a state variable that records the history of the system. Second, the Masing manifold reduces the set of equations governing the hysteretic behavior of a system to an analytical surface. The exploitation of these two advances has the potential for significant computational savings, and is being pursued in subsequent work.

Acknowledgements

The authors are thankful for the support of the National Science Foundation under Grant Number 1847130. Additionally, this material is based upon work supported by the U.S. Department of Energy, Office of Science, Office of Advanced Scientific Computing Research, Department of Energy Computational Science Graduate Fellowship under Award Number(s) DE-SC0021110. Lastly, this work was supported in part by the Big-Data Private-Cloud Research Cyberinfrastructure MRI-award funded by NSF under grant CNS-1338099 and by Rice University's Center for Research Computing (CRC).

Authors' Contributions

M. R. W. Brake was responsible for conceptualization, methodology, software, validation, formal analysis, investigation, resources, writing - original draft, writing - review and editing, visualization, supervision, and project administration. J. H. Porter was responsible for conceptualization, methodology, software, validation, formal analysis, investigation, data curation, writing - original draft, and writing - review and editing. M. M. Karpov was responsible for methodology, investigation, and visualization.

References

[1] H. G. D. Goyder and D. P. T. Lancereau. Methods for the measurement of non-linear damping and frequency in built-up structures. In *ASME International Design Engineering Technical Conferences IDETC/CIE*, Cleveland, OH, August 2017. doi:10.1115/DETC2017-67007.

[2] M. R. W. Brake, editor. *The Mechanics of Jointed Structures*. Springer, 2017. doi:10.1007/978-3-319-56818-8.

[3] M. R. W. Brake, C. W. Schwingshackl, and P. Reuß. Observations of variability and repeatability in jointed structures. *Mechanical Systems and Signal Processing*, 129:282–307, 2019. doi:10.1016/j.ymssp.2019.04.020.

[4] K. Holmberg and P. A. A. Erdemir. Global energy consumption due to friction in passenger cars. *Tribology International*, 47: 221–234, 2012. doi:10.1016/j.triboint.2011.11.022.

[5] K. Holmberg and A. Erdemir. Influence of tribology on global energy consumption, costs and emissions. *Friction*, 5:263–284, 2017. doi:10.1007/s40544-017-0183-5.

[6] D. Nowell, D. Dini, and D. A. Hills. Recent developments in the understanding of fretting fatigue. *Engineering Fracture Mechanics*, 73:207–222, 2006. doi:10.1016/j.engfracmech.2005.01.013.

[7] A. Fantetti, L. R. Tamatam, M. Volvert, I. Lawal, L. Liu, et al. The impact of fretting wear on structural dynamics: Experiment and simulation. *Tribology International*, 138:111–124, 2019. doi:10.1016/j.triboint.2019.05.023.

[8] Z.-B. Cai, Z.-Y. Li, M.-G. Yin, M.-H. Zhu, and Z.-R. Zhou. A review of fretting study on nuclear power equipment. *Tribology International*, 144:106095, 2020. doi:10.1016/j.triboint.2019.106095.

[9] M. R. W. Brake. Contact modeling across scales: From materials to structural dynamics applications. *Journal of Structural Dynamics*, 1:49–135, 2021. doi:10.25518/2684-6500.72.

[10] A. T. Mathis, N. N. Balaji, R. J. Kuether, A. R. Brink, M. R. W. Brake, et al. A review of damping models for structures with mechanical joints. *Applied Mechanics Reviews*, 72:040802, 2020. doi:10.1115/1.4047707.

[11] W. Chen, M. Jin, I. G. Lawal, M. R. W. Brake, and H. Song. Measurement of slip and separation in jointed structures with non-flat interfaces. *Mechanical Systems and Signal Processing*, 134:106325 (1–22), 2019. doi:10.1016/j.ymssp.2019.106325.

[12] M. Brons, T. A. Kasper, G. Chauda, S. W. B. Klaassen, C. W. Schwingshackl, et al. Experimental investigation of local dynamics in bolted lap joints using digital image correlation. *ASME Journal of Vibration and Acoustics*, 142:051114, 2020. doi:10.1115/1.4047699.

[13] W. Chen, D. Jana, A. Singh, M. Jin, M. Cenedese, et al. Measurement and identification of the nonlinear dynamics of a jointed structure using full-field data part I: Measurement of nonlinear dynamics. *Mechanical Systems and Signal Processing*, 166: 108401, 2022. doi:10.1016/j.ymssp.2021.108401.

[14] M. Jin, G. Kosova, M. Cenedese, W. Chen, A. Singh, et al. Measurement and identification of the nonlinear dynamics of a jointed structure using full-field data part II - nonlinear system identification. *Mechanical Systems and Signal Processing*, 166: 108402, 2022. doi:10.1016/j.ymssp.2021.108402.

[15] D. J. Segalman, D. L. Gregory, M. J. Starr, B. R. Resor, M. D. Jew, et al. *Handbook on Dynamics of Jointed Structures*. Technical Report SAND2009-4164. Sandia National Laboratories, Albuquerque, NM, 2009.

[16] T. Dreher, M. R. W. Brake, B. Seeger, and M. Krack. In situ, real-time measurements of contact pressure internal to jointed interfaces during dynamic excitation of an assembled structure. *Mechanical Systems and Signal Processing*, 160:107859, 2021. doi:10.1016/j.ymssp.2021.107859.

[17] R. M. Lacayo, L. Pesaresi, J. Groß, D. Fochler, J. Armand, et al. Nonlinear modeling of structures with bolted joints: a comparison of two approaches based on a time-domain and frequency-domain solver. *Mechanical Systems and Signal Processing*, 114:413–438, 2019. doi:10.1016/j.ymssp.2018.05.033.

[18] M. Ruan. *The Variability of Strains in Bolts and the Effecton on Preload in Jointed Structures*. Masters Dissertation. Rice University, Houston, TX., 2019.

[19] N. N. Balaji, W. Chen, and M. R. W. Brake. Traction-based multi-scale nonlinear dynamic modeling of bolted joints: Formulation, application, and trends in micro-scale interface evolution. *Mechanical Systems and Signal Processing*, 139:106615 (1–32), 2020. doi:10.1016/j.ymssp.2020.106615.

[20] A. R. Brink, R. J. Kuether, M. D. Fronk, B. L. Witt, and B. L. Nation. Contact stress and linearized modal predictions of as-built preloaded assembly. *ASME Journal of Vibration and Acoustics*, 142:051106, 2020. doi:10.1115/1.4046957.

[21] N. N. Balaji, T. Dreher, M. Krack, and M. R. W. Brake. Reduced order modeling for the dynamics of jointed structures through hyper-reduced interface representation. *Mechanical Systems and Signal Processing*, 149:107249, 2021. doi:10.1016/j.ymssp.2020.107249.

[22] J. H. Porter and M. R. W. Brake. Towards a predictive, physics-based friction model for the dynamics of jointed structures. *Mechanical Systems and Signal Processing*, 192:110210, 2023. doi:10.1016/j.ymssp.2023.110210.

[23] E. P. Petrov and D. J. Ewins. Analytical formulation of friction interface elements for analysis of nonlinear multiharmonic vibrations of bladed discs. *ASME Journal of Turbomachinery*, 125:364–371, 2002. doi:10.1115/1.1539868.

[24] J. Geisler and K. Willner. Modeling of jointed structures using zero thickness interface elements. *Proceedings in Applied Mathematics and Mechanics*, 7:4050009–4050010, 2007. doi:10.1002/pamm.200700227.

[25] S. Zucca, C. M. Firrone, and M. M. Gola. Modeling underplatform dampers for turbine blades: A refined approach in the frequency domain. *Journal of Vibration and Control*, 19:1087–1102, 2013. doi:10.1177/1077546312440809.

[26] D. Süß and K. Willner. Investigation of a jointed friction oscillator using the multiharmonic balance method. *Mechanical Systems and Signal Processing*, 52-53:73–87, 2015. doi:10.1016/j.ymssp.2014.08.003.

[27] L. Pesaresi, L. Salles, J. S. Green, and C. W. Schwingshackl. Modelling the nonlinear behaviour of an underplatform damper test rig for turbine applications. *Mechanical Systems and Signal Processing*, 85:662–679, 2017. doi:10.1016/j.ymssp.2016.09.007.

[28] M. Krack. Nonlinear modal analysis of nonconservative systems: Extension of the periodic motion concept. *Computers & Structures*, 154:59–71, 2015. doi:10.1016/j.compstruc.2015.03.008.

[29] J. J. Hollkamp and R. W. Gordon. Reduced-order models for nonlinear response prediction: Implicit condensation and expansion. *Journal of Sound and Vibration*, 318:1139–1153, 2008. doi:10.1016/j.jsv.2008.04.035.

[30] H. Festjens, G. Chevallier, and J.-L. Dion. A numerical tool for the design of assembled structures under dynamic loads. *International Journal of Mechanical Sciences*, 75:170–177, 2013. doi:10.1016/j.ijmecsci.2013.06.013.

[31] R. M. Lacayo and M. S. Allen. Updating structural models containing nonlinear Iwan joints using quasi-static modal analysis. *Mechanical Systems and Signal Processing*, 114:413–438, 2019. doi:10.1016/j.ymssp.2018.08.034.

[32] N. N. Balaji and M. R. W. Brake. An efficient quasi-static non-linear modal analysis procedure generalizing Rayleigh quotient stationarity for non-conservative dynamical systems. *Computers and Structures*, 230:106184 (1–16), 2020. doi:10.1016/j.compstruc.2019.106184.

[33] M. Krack, L. Panning-von Scheidt, and J. Wallaschek. A high-order harmonic balance method for systems with distinct states. *Journal of Sound and Vibration*, 332:5476–5488, 2013. doi:10.1016/j.jsv.2013.04.048.

[34] J. Armand, L. Pesaresi, L. Salles, C. Wong, and C. W. Schwingshackl. A modelling approach for the nonlinear dynamics of assembled structures undergoing fretting wear. *Proceedings of the Royal Society A*, 475:20180731, 2019. doi:10.1098/rspa.2018.0731.

[35] Y. Sun, J. Yuan, L. Pesaresi, E. Denimal, and L. Salles. Parametric study and uncertainty quantification of the nonlinear modal properties of frictional dampers. *ASME Journal of Vibration and Acoustics*, 142:051102, 2020. doi:10.1115/1.4046953.

[36] J. Yuan, A. Fantetti, E. Denimal, S. Bhatnagar, L. Pesaresi, et al. Propagation of friction parameter uncertainties in the nonlinear dynamic response of turbine blades with underplatform dampers. *Mechanical Systems and Signal Processing*, 156: 107673, 2021. doi:10.1016/j.ymssp.2021.107673.

[37] J. H. Porter, N. N. Balaji, C. R. Little, and M. R. W. Brake. A quantitative assessment of the model form error of friction models across different interface representations for jointed structures. *Mechanical Systems and Signal Processing*, 163:108163, 2022. doi:10.1016/j.ymssp.2021.108163.

[38] G. Masing. Self-stretching and hardening for brass. *Proceedings of the Second International Congress for Applied Mechanics*, pages 332–335, 1926.

[39] D. J. Segalman. A four-parameter Iwan model for lap-type joints. *ASME Journal of Applied Mechanics*, 72:752–760, 2005. doi:10.1115/1.1989354.

[40] A. T. Mathis, N. N. Balaji, R. J. Kuether, A. R. Brink, M. R. W. Brake, et al. A review of damping models for structures with mechanical joints. *Applied Mechanics Reviews*, 72:040802, 2020. doi:10.1115/1.4047707.

[41] M. S. Allen, R. M. Lacayo, and M. R. W. Brake. Quasi-static modal analysis based on implicit condensation for structures with nonlinear joints. In *International Conference on Noise and Vibration Engineering*, Leuven, Belgium, September 2016.

[42] N. N. Balaji. *Dissipative Dynamics of Bolted Joints.* Ph.D. thesis, Rice University, Houston, Texas, 2021.

[43] R. D. Mindlin and H. Deresiewicz. Elastic spheres in contact under varying oblique forces. *ASME Journal of Applied Mechanics*, 20:327–344, 1953. doi:10.1115/1.4010702.

[44] W. C. Hurty. Dynamic analysis of structural systems using component modes. *AIAA Journal*, 3:678–685, 1960. doi:10.2514/3.2947.

[45] R. R. Craig and M. C. C. Bampton. Coupling of substructures for dynamic analyses. *AIAA Journal*, 6(7):1313–1319, 1968. doi:10.2514/3.4741.

[46] T. M. Cameron and J. H. Griffin. An alternating frequency/time domain method for calculating the steady-state response of nonlinear dynamic systems. *ASME Journal of Applied Mechanics*, 56:149–154, 1989. doi:10.1115/1.3176036.

[47] J. Guillen and C. Pierre. An Efficient, Hybrid, Frequency-Time Domain Method for The Dynamics of Large-Scale Dry-Friction Damped Structural Systems. In F. Pfeiffer and C. Glocker, editors, *IUTAM Symposium on Unilateral Multibody Contacts*, Solid Mechanics and Its Applications, pages 169–178. Springer Netherlands, 1999. ISBN 978-94-011-4275-5. doi:10.1007/978-94-011-4275-5_17.

[48] M. Krack and J. Groß. *Harmonic Balance for Nonlinear Vibration Problems*. Mathematical Engineering. Springer International Publishing, 2019. ISBN 978-3-030-14022-9. doi:10.1007/978-3-030-14023-6.